scientific reports

Check for updates

OPEN

Occurrence characteristics and amplitude-frequency relationship of the Pc5 ULF waves from 3 decades of GOES data

Fadil Inceoglu[1,2]✉ & Paul T. M. Loto'aniu[1,2]

We investigate the occurrence characteristics and amplitude-frequency relationships of Pc5 ultra-low frequency (ULF) waves (1.67–6.7 mHz) using 30 years of GOES magnetic field data (1995–2025) from GOES-8 to GOES-18. An enhanced CLEAN algorithm, employing iterative Hanning peak model fitting and subtraction, identified 27,279 radial, 26,145 azimuthal, and 31,259 parallel wave events in the Mean Field-Aligned coordinate system. Radial and parallel waves exhibit peak amplitudes between 9–15 MLT, driven by solar wind dynamic pressure, while azimuthal and parallel components dominate in the 15–21 MLT sector, consistent with Kelvin-Helmholtz instability. Strong power-law relationships ($R^2 \geq 0.85$) between amplitude and frequency are observed for radial and azimuthal components in dawn and dusk sectors, with weaker correlations for the parallel component ($R^2 \leq 0.24$). These relationships vary with solar wind conditions, with radial components showing robust power-law fits under strong and moderate conditions ($R^2 \geq 0.93$). ULF wave occurrence rates peak during solar maxima, correlating strongly with solar wind parameters ($R^2 \geq 0.73$), and exhibit quasi-biennial oscillations (QBOs)–short-term (1.5–4 year) modulations linked to solar dynamo processes. High-pass filtered data show strong correlations with dynamic pressure ($R^2 \geq 0.85$). These findings resolve discrepancies in prior studies, highlighting the interplay of solar cycle, QBOs, and MLT-dependent drivers in Pc5 ULF wave dynamics, with implications for radiation belt dynamics and space weather forecasting.

Keywords Pc5 ULF waves, GOES satellites, Quasi-biennial oscillations (QBOs)

Ultra Low Frequency (ULF) waves in Earth's magnetosphere, observed between approximately 1.67 and 6.7 mHz, are classified as continuous pulsations in the Pc5 band[1,2]. These waves are primarily driven by solar wind-magnetosphere interactions, with the solar wind acting as the dominant external energy source[3–5]. Pc5 activity is often enhanced during intervals of elevated solar wind dynamic pressure and high-speed streams, which create favorable upstream conditions for wave excitation. Several specific generation mechanisms have been identified. Variations in solar wind dynamic pressure can directly compress the magnetopause, driving global compressional oscillations that couple to field line resonances. Velocity shear along the magnetospheric flanks excites the Kelvin-Helmholtz instability (KHI), producing toroidal shear Alfvén waves[6–12]. In addition, internal magnetospheric processes such as drift-bounce resonance of ring current ions can sustain Pc5 oscillations[13,14].

Beyond these well-known drivers, other important mechanisms contribute to Pc5 wave excitation but are less frequently highlighted in statistical studies. These include cavity and waveguide modes. In the cavity mode, energy injected into the magnetosphere excites global oscillations at the cavity's eigenfrequencies, which then efficiently couple to magnetic field lines and produce characteristic field line resonance signatures. The waveguide mode is similar, but the cavity remains open downtail, allowing compressional waves to propagate antisunward along the magnetospheric flanks at the system's natural frequencies[15].

Additional mechanisms include surface eigenmodes at the magnetopause and plasmapause, which arise from steep plasma density gradients and excite compressional Pc5 waves[16]. Magnetospheric breathing modes, directly driven by quasi-periodic solar wind dynamic pressure pulses, have a characteristic frequency range of roughly 0.2–5.0 mHz[17–19]. These density pulses are not necessarily as sharp as interplanetary shocks, which are usually considered broadband drivers that excite intrinsic magnetospheric eigenmodes. Compressional cavity

[1]Cooperative Institute for Research in Environmental Sciences, University of Colorado Boulder, Boulder, CO, USA. [2]National Centers for Environmental Information, National Oceanic and Atmospheric Administration, Boulder, CO, US. ✉email: fadil.inceoglu@colorado.edu

and waveguide modes, by contrast, typically occur on 2–5 min timescales and can also couple efficiently into field line resonances[17]. Finally, transient ion foreshock phenomena–such as foreshock cavities and hot flow anomalies–produce upstream compressional perturbations that can couple into Pc5 ULF waves within the magnetosphere[20].

In field-aligned coordinates (r, ϕ, $\|$), Pc5 ULF wave magnetic fields are typically observed as a combination of poloidal (B_r), toroidal (B_ϕ), and compressional field-aligned ($B_\|$) modes, with the poloidal and toroidal components often dominating the wave power. Mode conversion–particularly between poloidal and toroidal modes–is believed to play a significant role, and there is ongoing research into the solar wind and magnetospheric conditions that drive these wave excitations. Studying Pc5 waves is critical for space weather research, as they have been shown to influence the dynamics of relativistic electrons in Earth's radiation belts (e.g., see the review[21]).

The Kelvin-Helmholtz instability (KHI) and variations in solar wind dynamic pressure both generate fast mode waves in the magnetosphere, which can couple to shear Alfvén waves (often observed as toroidal Pc5 modes) depending on the magnetic field configuration and cold plasma distribution[8,22]. Solar wind dynamic pressure variations are also associated with compressional Pc5 wave activity, driving global oscillations that may couple to field line resonances[15]. These processes highlight the complex interplay between external drivers and internal magnetospheric conditions in Pc5 ULF wave excitation.

In our previous study[23], we analyzed the statistical properties of ULF waves at geostationary orbit. In the present study, we build on that work using an improved methodology to examine wave amplitude as a function of wave frequency, space weather conditions, and magnetic local time (MLT) sectors.

The wave mode, frequency, power, MLT occurrence, and duration all influence the strength and nature of wave-particle interactions, and thus the role of ULF waves in accelerating relativistic electrons. Numerous statistical studies have been conducted to characterize the global occurrence, spectral features, spatial distribution, and temporal behavior of Pc5 ULF waves[24–26].

Large-scale statistical studies are crucial for advancing our understanding of wave generation mechanisms and occurrence patterns, including the temporal variability of Pc5 wave activity. However, most such studies are limited to datasets covering only up to 13 years of magnetic field measurements[10,25–34].

Using magnetic field data from GOES-2 and GOES-3 between 1978 and 1980, it was found that azimuthal Pc5 ULF waves occur more frequently in the dawn sector than in the dusk sector, a distribution attributed to the influence of the interplanetary magnetic field on the Kelvin-Helmholtz instability[27]. However, more recent studies have shown that this dawn-dusk asymmetry originates from internal magnetospheric conditions, such as the local time dependence of radial mass density variations and the associated gradient of standing Alfvén wave frequencies, rather than IMF-driven KHI[35]. In contrast, compressional radial Pc5 ULF waves tend to occur under magnetically disturbed conditions, particularly on the dusk side. Long-duration Pc5 waves ($\geq$ 3 h) are most commonly observed in the dayside sector, while short-duration waves predominantly occur in the afternoon sector (13–18 MLT)[27]. A subsequent study using GOES-8 magnetic field data from 2001 suggested that oscillations in solar wind dynamic pressure are a primary driver of Pc5 ULF waves at geosynchronous orbit, with azimuthal power peaking in the pre-midnight sector–likely due to substorm activity[10]. The same study reported that compressional radial waves increase both in the noon sector (around 12 MLT) and the night sector, consistent with pressure-driven radial displacements of magnetic field lines[10]. In contrast, an analysis of GOES-15 data from 2013 to 2016 showed that compressional radial Pc5 ULF waves peaked in the night sector (20–22 MLT)[25]. The toroidal mode followed a similar MLT pattern, whereas the poloidal mode exhibited enhanced occurrence in the dayside sector between 10 and 13 MLT[25].

The discrepancies among these studies may stem, in part, from differences in the phases of the solar cycle during which the observations were made. For instance, the GOES-2 and GOES-3 study corresponds to the ascending phase of solar cycle 21, while the GOES-8 analysis was conducted during the solar maximum of cycle 23, a weaker cycle than 21. The GOES-15 study, by contrast, spans both the maximum and descending phase of solar cycle 24. More recently, we compiled a database of Pc5 ULF waves using the CLEAN algorithm, based on 30 years of magnetic field data from GOES-8 through GOES-17[23]. That study identified Pc5 ULF waves in all three components of the Mean Field-Aligned (MFA) coordinate system–radial, azimuthal, and parallel. Results showed that while radial wave occurrences peaked in the night sector (19–23 MLT), the largest amplitudes were observed on the dayside between 10 and 13 MLT. The azimuthal and parallel components peaked between 21–23 and 13–23 MLT, respectively[23]. Additionally, the azimuthal component exhibited higher amplitudes across a broad MLT range (03–21 MLT), with enhanced regions around both flanks, while the parallel component showed stronger wave amplitudes primarily between 03 and 18 MLT[23].

In this study, we generate a new Pc5 ULF wave database using an enhanced version of the CLEAN algorithm (see Methods), based on magnetic field data from GOES-8 through GOES-18 and spanning approximately 30 years. We analyze amplitude-frequency relationships for the radial, azimuthal, and parallel components across magnetic local time sectors and under varying solar wind conditions. Furthermore, we examine the temporal evolution of ULF wave occurrence rates in the MFA coordinate system as a function of solar wind speed, dynamic pressure, and total magnetic field, across multiple time scales.

Results

Throughout the study period, from 1 July 1995 to 10 May 2025, we selected the three highest-amplitude Pc5 ULF wave events within each sliding 1-h window from the ULF wave database we generated using 30 years of GOES magnetic field data. These amplitudes were identified using the CLEAN algorithm, which operates in the frequency domain based on the Fast Fourier Transform (FFT). During the entire interval, we identified 27,279 events in the radial component (B_r), 26,145 in the azimuthal component (B_ϕ) and 31,259 in the parallel component ($B_{||}$). These updated counts differ slightly from earlier work[23] because the revised analysis applies

stricter amplitude thresholds, refined peak fitting/removal, and retains only the three strongest peaks per FFT window, resulting in a smaller but more robust event set.

The amplitudes of the selected Pc5 ULF waves as a function of frequency and magnetic local time (MLT) are shown in the top row of Fig. 1. In the radial component (B_r), amplitudes above ∼15 nT are concentrated between 9 and 15 MLT, with frequencies extending up to 5 mHz (Fig. 1a). Additional amplitude enhancements in the range of ∼5–15 nT are observed between 3 and 9 MLT, with smaller but still detectable values between 18 and 21 MLT.

For the azimuthal component (B_ϕ), amplitudes exceeding ∼10 nT span the 12 and 18 MLT sector across much of the frequency range, with additional activity between 3 and 9 MLT (Fig. 1b). In contrast to B_r, a relative decrease in amplitudes is evident between 9 and 12 MLT, where amplitudes remain below ∼10 nT.

The parallel component ($B_{||}$) shows amplitudes up to ∼15 nT concentrated at low frequencies (< 3 mHz) between 9 and 15 MLT, while most other detections between 15 and 21 MLT remain in the 5-15 nT range across the full frequency band (Fig. 1c). Additional detections between 3 and 9 MLT are generally limited to frequencies below 4 mHz, while the 15–21 MLT interval extends to higher frequencies than the 3–9 MLT interval (Fig. 1b, c). In addition to the weak overall correlation, the parallel component in the day sector shows a localized enhancement around 4–5 mHz. This peak deviates from the power-law trend and may indicate a distinct source mechanism, such as cavity or waveguide modes.

Another clear pattern is that between 18 and 24 MLT for the parallel component, amplitudes drop below ∼ 5 nT above 4 mHz. In the 0–6 MLT interval, the azimuthal component shows almost no detections, whereas the radial component retains elevated amplitudes in the 3–9 MLT sector. Similar frequency-dependent reductions are otherwise observed in the parallel and azimuthal components at 18–24 MLT (Figs. 1a–c).

Next, we examine the relationship between the number of identified Pc5 ULF waves and their distribution in MLT and frequency, as shown in the bottom row of Fig. 1. Across all three components in the Mean Field-Aligned (MFA) coordinate system, ULF waves are detected throughout the entire MLT range (Fig. 1d–f).

For the radial component (B_r), the largest concentrations of detections occur between 18 and 6 MLT, particularly for frequencies below 3 mHz (Fig. 1d). Interestingly, although the 9–15 MLT interval is where the highest-amplitude waves are observed (Fig. 1a), it does not exhibit an elevated number of detections. Above 3 mHz, B_r detections become more concentrated between 3–9 and 15–18 MLT, extending up to 7 mHz.

The azimuthal component (B_ϕ) shows a different distribution: below 3 mHz, detections are spread broadly across both 18–6 MLT and 9–15 MLT. At higher frequencies (3–7 mHz), the detections become concentrated between 12–18 MLT, with very limited activity between 3 and 9 MLT (Fig. 1e). This component also shows a relatively continuous presence of waves up to 7 mHz.

The parallel component ($B_{||}$) exhibits a similar distribution to the azimuthal component, with low-frequency detections spread across 18–6 MLT and 9–15 MLT, but with a preference for 15–21 MLT at higher frequencies (3–7 mHz), while again showing minimal detections between 3 and 9 MLT (Fig. 1f).

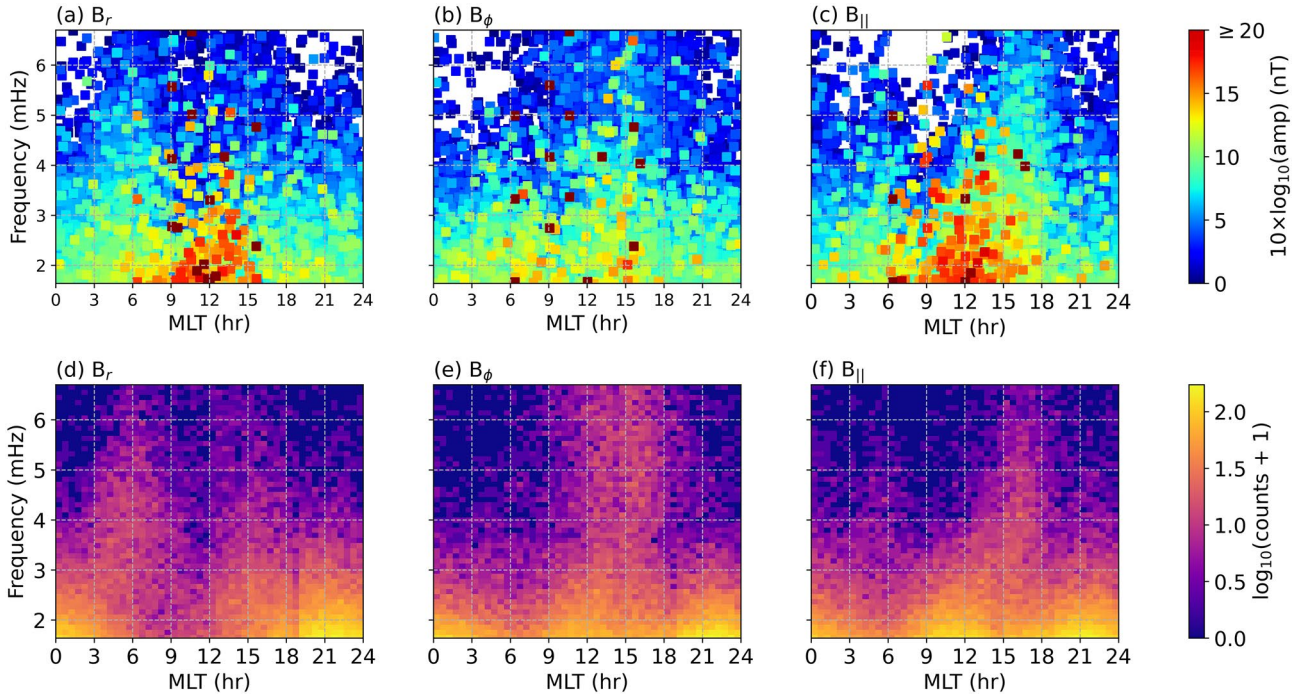

Fig. 1. The top row shows the Pc5 ULF waves found in the radial (**a**), azimuthal (**b**), and parallel (**c**) components in the MFA coordinate frame. The logarithmic amplitudes are given as a function of frequency and MLTs. The bottom row shows the distributions of the frequencies of the ULF waves as functions of MLTs in the (**d**) radial, (**e**) azimuthal, and (**f**) parallel components in the MFA coordinate frame.

To investigate the relationship between amplitude and frequency in the identified Pc5 ULF waves as a function of MLT sector, we first divided the data into four distinct sectors: (i) dawn (3–9 MLT), (ii) day (9–15 MLT), (iii) dusk (15–21 MLT), and (iv) night (21–3 MLT) (Fig. 2).

In the 3–9 MLT interval (dawn sector), the radial component exhibits a strong power-law relationship between central frequency and median amplitude, with amplitudes increasing as frequency decreases ($R^2 = 0.97$; Fig. 2a). The azimuthal component also follows a clear power-law trend, though less tightly ($R^2 = 0.85$; Fig. 2e), with some deviations at specific frequencies. The parallel component, however, shows only a weak inverse power-law dependence between amplitude and frequency ($R^2 = 0.24$; Fig. 2i).

In the 9–15 MLT interval (day sector), the radial component still follows a power-law relationship, though weaker than in 3–9 MLT ($R^2 = 0.87$; Fig. 2b). The azimuthal component shows a very weak power-law relationship between amplitude and frequency ($R^2 = 0.29$; Fig. 2f), while the parallel component displays no meaningful relationship ($R^2 = 0.08$; Fig. 2j).

In the 15–21 MLT interval (dusk sector), the radial component again shows a strong power-law trend ($R^2 = 0.89$; Fig. 2c). The azimuthal component similarly demonstrates a strong relationship ($R^2 = 0.89$; Fig. 2g). The parallel component shows a moderate inverse power-law trend, weaker than the radial and azimuthal components but still evident ($R^2 = 0.76$; Fig. 2k).

In the 21–3 MLT interval (night sector), the radial component exhibits a more moderate (weaker) power-law relationship compared to the other intervals ($R^2 = 0.76$; Fig. 2d). The azimuthal component also shows a moderate relationship ($R^2 = 0.71$; Fig. 2h). In contrast, the parallel component shows only a very weak amplitude-frequency dependence ($R^2 = 0.34$; Fig. 2l), similar to the 3–9 MLT interval.

We emphasize that Figs. 1 and 2 represent different statistical measures. Figure 1 highlights the largest individual amplitudes, dominated by fewer but stronger noon-sector events, while Fig. 2 reflects median amplitudes, which are elevated in the dawn sector due to numerous moderate-strength events (see Methods). This explains the apparent discrepancy between the two figures.

In addition to examining the amplitude-frequency relationships across different MLT intervals, we also analyzed these relationships for each component in the MFA coordinate system under varying solar wind conditions (see Methods).

For the radial component, a clear power-law relationship between median amplitudes and center frequencies of the ULF waves is present under all solar wind conditions. The relationship is strongest during moderate solar

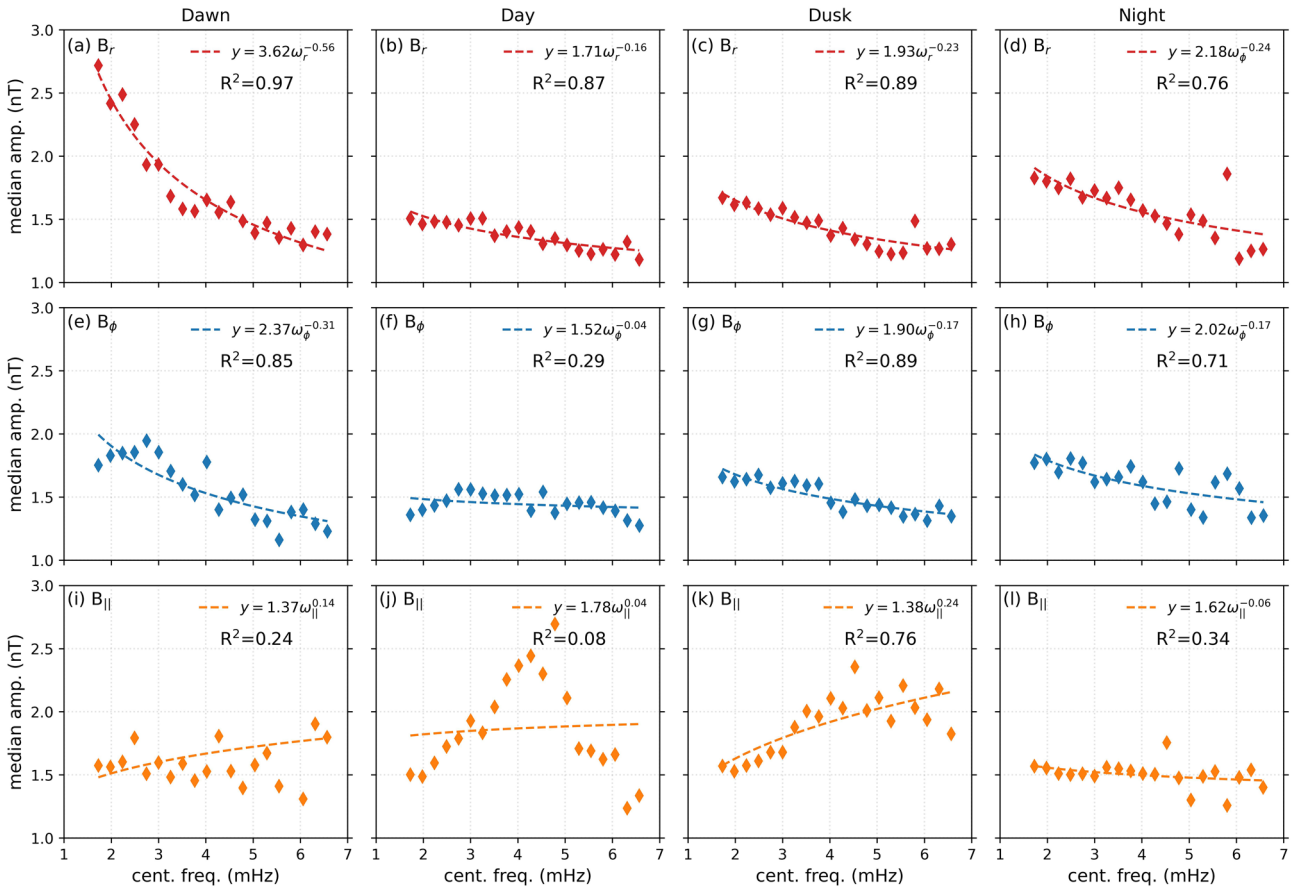

Fig. 2. Relationship between the amplitudes and frequency centroids in the dawn, day, dusk, and night sectors in the radial (top panel), azimuthal (middle panel), and parallel (bottom panel) components in the MFA coordinate frame.

wind conditions ($R^2 = 0.94$), slightly weaker but still highly correlated during strong solar wind conditions ($R^2 = 0.93$), and somewhat reduced during weak solar wind conditions ($R^2 = 0.82$; Fig. 3a–c).

For the azimuthal component, the amplitude-frequency relationship varies more noticeably with solar wind conditions. It shows only a limited correlation under strong solar wind conditions ($R^2 = 0.44$), becomes more pronounced under moderate conditions ($R^2 = 0.63$), and decreases slightly under weak conditions ($R^2 = 0.57$; Fig. 3d–f).

For the parallel component, no meaningful power-law relationship is observed under strong solar wind conditions ($R^2 = 0.03$), with large deviations from any trend. Under moderate solar wind conditions, the relationship strengthens to a clear inverse power-law ($R^2 = 0.74$), while during weak solar wind conditions the inverse trend persists but the correlation is low ($R^2 = 0.13$; Fig. 3g–i).

We analyze the temporal variations in Pc5 ULF wave occurrence rates, defined as the fraction of valid 1-h intervals containing Pc5 detections normalized by the total number of available daily records per year (see Methods for details). This metric spans 30 years, covering two complete solar cycles (1996–2025) (Fig. 4). We further examine their covariations with yearly averaged solar wind dynamic pressure, the GSM B_z magnetic field component, and solar wind speed.

The occurrence rates in the radial, azimuthal, and parallel MFA components vary in phase with both solar wind parameters and the solar cycle, peaking during solar maxima and reaching minima during solar minima (Fig. 4a–c).

For solar cycle 23 (1996–2009), the ULF wave occurrence rates in the radial, azimuthal, and parallel components show moderate correlations with solar wind dynamic pressure ($R^2r = 0.73$, $R^2\phi = 0.75$, $R^2|| = 0.73$), moderate correlations with the GSM B_z magnetic field magnitude ($R^2r = 0.70$, $R^2\phi = 0.71$, $R^2|| = 0.70$), and moderate correlations with the solar wind speed ($R^2r = 0.72$, $R^2\phi = 0.74$, $R^2_{||} = 0.71$).

For solar cycle 24 (2009–2020), the ULF wave occurrence rates in the radial component show a moderate correlation ($R^2r = 0.70$), while the azimuthal and parallel components exhibit strong correlations with

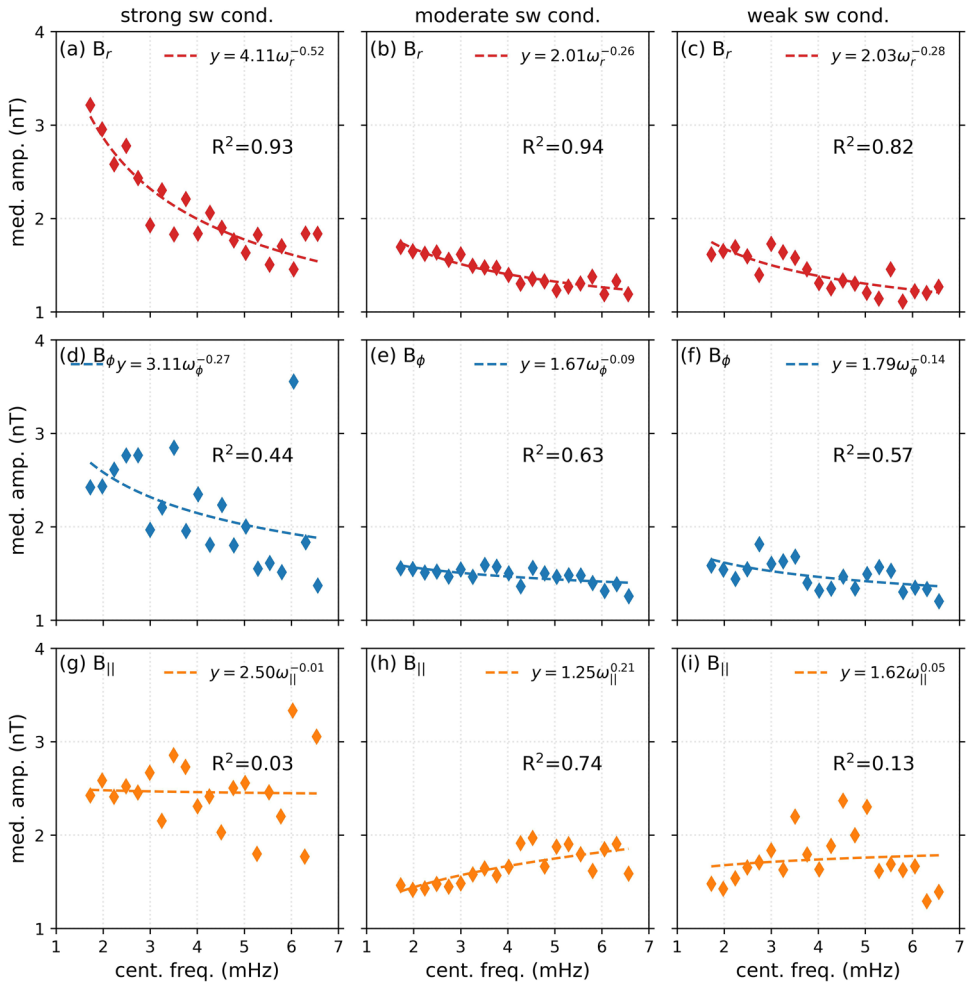

Fig. 3. Relationship between the amplitudes and frequency centroids in strong, moderate, and weak solar wind conditions in the radial (top panel), azimuthal (middle panel), and parallel (bottom panel) components in the MFA coordinate frame. Note that the y-axis limits for the moderate and weak solar wind conditions are half of those in the strong solar wind conditions.

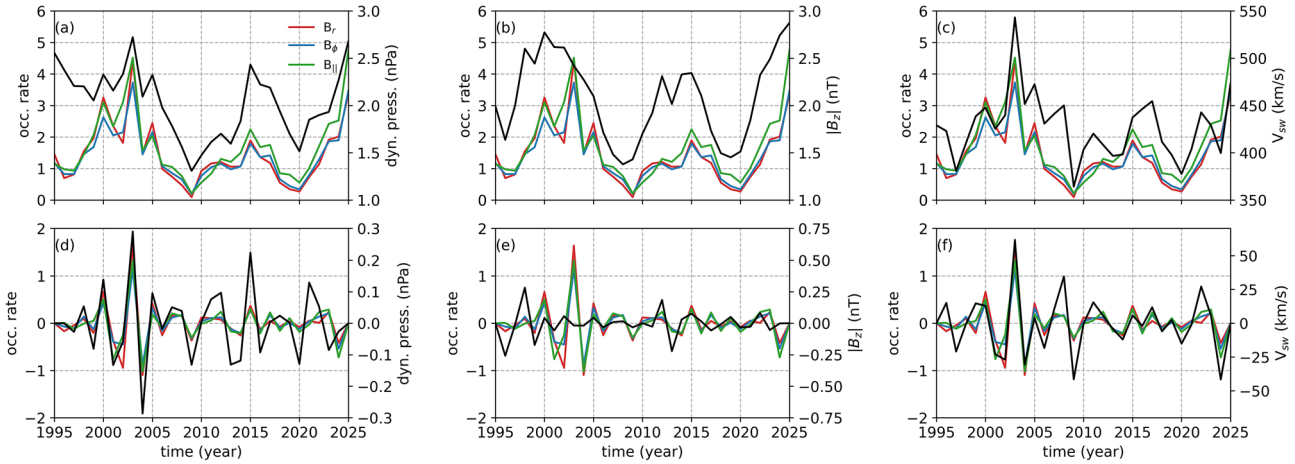

Fig. 4. The top row shows the occurrence rates of Pc5 ULF waves in the radial (red), azimuthal (blue), and parallel (green) components in the MFA coordinate system, along with solar wind dynamic pressure (panels a and d), the magnitude of the GSM B_z component ($|B_z|$) of the magnetic field (panels b and e), and solar wind speed (panels c and f). The bottom row presents the same parameters but high-pass filtered using a cut-off frequency of (1/5) year^{-1}. Note that the dynamic pressure, the magnitude of the GSM B_z ($|B_z|$), and solar wind speed are plotted on the secondary y-axis (right side) in each subplot.

solar wind dynamic pressure ($R^2\phi = 0.81$, $R^2|| = 0.90$). The occurrence rates of the radial and azimuthal components show strong correlations with the GSM B_z magnetic field magnitude ($R^2r = 0.84$, $R^2\phi = 0.78$), whereas the parallel component shows a moderate correlation with GSM B_z magnitude ($R^2|| = 0.73$). All three components exhibit moderate to strong correlations with solar wind speed ($R^2r = 0.74$, $R^2\phi = 0.83$, $R^2_{||} = 0.77$).

A notable feature in the temporal evolution of ULF wave occurrence rates and solar wind parameters is a multi-peak structure, with higher amplitudes during solar maxima and lower amplitudes during solar minima. To investigate these shorter-term variations, we applied a fifth-order high-pass Butterworth filter with a cutoff frequency of 1/5 year^{-1} to remove the long-term trend (see Methods).

For solar cycle 23 (1996–2009), the high-pass filtered ULF wave occurrence rates in the radial, azimuthal, and parallel components show strong correlations with solar wind dynamic pressure ($R^2r = 0.93$, $R^2\phi = 0.98$, $R^2|| = 0.96$), weak correlations with the GSM B_z magnetic field magnitude ($R^2r = 0.12$, $R^2\phi = 0.16$, $R^2|| = 0.06$), and strong correlations with solar wind speed ($R^2r = 0.84$, $R^2\phi = 0.86$, $R^2_{||} = 0.86$).

For solar cycle 24 (2009–2020), the high-pass filtered ULF wave occurrence rates maintain strong correlations with solar wind dynamic pressure for the radial, azimuthal, and parallel components ($R^2r = 0.91$, $R^2\phi = 0.89$, $R^2|| = 0.85$). Correlations with the GSM B_z component magnitude are weak for all three components ($R^2r = 0.33$, $R^2\phi = 0.34$, $R^2|| = 0.47$). Correlations with solar wind speed remain strong for the radial and azimuthal components ($R^2r = 0.78$, $R^2\phi = 0.82$), while the parallel component shows a moderate correlation ($R^2_{||} = 0.74$).

Discussion

In this study, we investigated the amplitude-frequency relationships and occurrence characteristics of Pc5 ULF waves across 3–9 MLT, 9–15 MLT, 15–21 MLT, and 21–3 MLT sectors, as well as under weak, moderate, and strong solar wind conditions. Using a Pc5 ULF wave database generated from 30 years of GOES magnetic field data (1995–2025) with an enhanced CLEAN algorithm[23], we selected the three highest-amplitude Pc5 ULF waves within each sliding 1-h window to analyze their properties in the radial (B_r), azimuthal (B_ϕ), and parallel ($B_{||}$) components of the Mean Field-Aligned (MFA) coordinate system.

Compared to our earlier study[23], the present work shows minor differences in the detailed MLT distributions, such as the absence of the reduced activity near 24 MLT and the previously noted increase in detection rates in the parallel component near 19 MLT. These differences arise primarily from methodological refinements introduced in this work. First, the current analysis treats MLT cyclically, eliminating the artificial drop in detections near the 24–0 MLT boundary seen in the earlier study. Second, only the three highest-amplitude peaks per FFT window are retained here, whereas the previous study counted all identified peaks, including marginal smaller detections. Finally, more conservative amplitude thresholds, improved Hanning peak fitting, and stricter Monte Carlo significance testing were applied. These refinements reduce the number of weaker or spurious detections, yielding a cleaner and more robust event catalog while maintaining consistency in the broader spatial-temporal patterns of Pc5 ULF activity.

Our results align with previous studies, showing that low-frequency Pc5 waves (< 3 mHz) have their highest concentrations of detections between 18–6 MLT, likely driven by substorm onsets that inject energetic particles and perturb magnetic field lines[25,36–38]. At higher frequencies (3–7 mHz), the radial component exhibits

enhanced detections between 3–9 MLT and 15–18 MLT, while the azimuthal and parallel components peak between 12–16 MLT. This dusk-flank preference is consistent with Kelvin-Helmholtz instability (KHI), which develops most efficiently along the magnetospheric flanks where velocity shear between the solar wind and magnetospheric plasma is strongest[39]. KH surface waves primarily excite azimuthal (toroidal) and field-aligned (parallel) oscillations through tangential boundary displacements and compressional coupling, rather than purely radial displacements. Moreover, KHI occurrence itself is modulated by seasonal and diurnal variations in dipole tilt, which alter magnetic tension at the magnetopause and further enhance dusk-flank asymmetries in wave growth[40]. These spatial and polarization patterns are broadly consistent with earlier statistical analyses of Pc4-Pc5 waves and their solar wind drivers[41].

These patterns are supported by moderate correlations with solar wind speed ($R^2 \geq 0.72$ across components in both solar cycles), which enhances KHI activity during high-speed streams. However, the highest-amplitude waves are observed between 9 and 15 MLT, particularly in the radial and parallel components, likely due to enhanced solar wind dynamic pressure buffeting the magnetosphere near local noon[23]. This buffeting amplifies radial displacements and poloidal oscillations, increasing wave amplitudes in the radial and parallel components, respectively. This distinction also explains why the largest amplitudes occur between 09–15 MLT while occurrence rates peak on the nightside: dayside activity is dominated by fewer but stronger dynamic-pressure-driven events, whereas nightside activity reflects more numerous but generally lower-amplitude substorm-related oscillations[23,36–38].

The amplitude-frequency relationships reveal distinct patterns across MLT sectors. In the dawn and dusk sectors, the radial and azimuthal components exhibit strong power-law relationships ($R^2 \geq 0.79$), with amplitudes increasing as frequency decreases, suggestive of field line resonances or magnetospheric cavity modes excited by solar wind interactions[6,8]. The parallel component, however, shows a moderate inverse power-law relationships ($R^2 \leq 0.56$), indicating that compressional modes are less frequency-dependent. In the day sector, the radial component maintains a strong power-law fit ($R^2 = 0.91$), but the azimuthal and parallel components show weak correlations ($R^2 \leq 0.23$), possibly due to competing influences from solar wind dynamic pressure and mode conversion processes[12].

The temporal evolution of ULF wave occurrence rates shows a strong in-phase relationship with solar wind parameters (dynamic pressure, GSM B_z magnitude, speed) and the solar cycle, peaking during solar maxima and declining during minima. This is consistent with prior studies linking ULF wave activity to solar cycle phases[42–45]. Stronger correlations during solar cycle 24 (e.g., $R^2_{||} = 0.90$ for dynamic pressure) may reflect the prevalence of high-speed solar wind streams from coronal holes, which enhance KHI and pressure-driven wave activity[45]. Additionally, we find a robust in-phase relationship between ULF wave occurrence rates and quasi-biennial oscillations (QBOs) in solar wind parameters, which are more pronounced than the 11-year solar cycle signal[46,47]. These QBOs, likely originating from dynamo processes at the base of the solar convection zone[48–50], modulate solar wind dynamic pressure and IMF, driving periodic enhancements in magnetospheric wave activity. The high-pass filtered data further reveal short-term (1.5-4 year) variations, with strong correlations to solar wind dynamic pressure ($R^2 \geq 0.85$), suggesting that QBOs play a significant role in ULF wave variability.

The 30-year dataset resolves discrepancies in prior studies, which were limited to shorter timeframes (e.g., 2-4 years) and different solar cycle phases[10,25,27]. For instance, the nightside peak in radial wave occurrences (19–23 MLT) aligns with GOES-15 findings[25], while dayside amplitude peaks (9–15 MLT) are consistent with GOES-8 results[10], reflecting solar wind buffeting effects. The extended dataset highlights the interplay of solar cycle phase, QBOs, and MLT-dependent wave modes, providing a comprehensive view of Pc5 ULF wave dynamics.

The nodal structure of Pc5 standing Alfvén waves may lead to underestimation of their occurrence and amplitudes in magnetic field data near the magnetic equator, where odd-mode waves (e. g. fundamental modes), exhibit minimal magnetic perturbations[51]. We note that reliably separating odd and even harmonics is not feasible at geostationary orbit with single-satellite data, since odd modes exhibit minimal magnetic perturbations near the equator. Following earlier large-scale surveys[10,25,26,28–34], we therefore treat Pc5 detections as an integrated population while acknowledging that harmonic structure may influence detection sensitivity. Since GOES satellites are located slightly off the magnetic equator, they may detect these waves with reduced amplitudes, potentially affecting the occurrence statistics and the frequency-amplitude relationships calculated for different sectors and solar wind conditions. This detection sensitivity underscores the importance of considering wave harmonic structures in interpreting our magnetic field-based results.

In conclusion, our findings underscore the complex interplay of solar wind-magnetosphere interactions in driving Pc5 ULF waves. The strong power-law relationships in the radial and azimuthal components, coupled with MLT-dependent occurrence patterns, highlight the roles of KHI and solar wind dynamic pressure buffeting in wave excitation. We note, however, that these are not the only generation mechanisms at play; cavity and waveguide modes, as well as magnetospheric breathing oscillations, can also be excited under varying solar wind conditions[15,17–19]. The in-phase relationship with the solar cycle and QBOs suggests that long-term solar variability significantly modulates ULF wave activity. Future studies should further investigate how the observed resonant frequencies relate to both intrinsic magnetospheric eigenmodes and periodicities imposed by recurrent solar wind structures.

Methods

Data preprocessing and Pc5 ULF wave detection via the CLEAN algorithm

The transformation of magnetic field data into the Mean Field-Aligned (MFA) coordinate system, comprising radial (B_r), azimuthal (B_ϕ), and parallel ($B_{||}$) components, was performed using a methodology consistent with our previous study[23]. To determine the magnetic field baseline for this rotation, a 30-min running average was applied to the 1-min cadence data from GOES-8 to GOES-18, spanning July 1, 1995, to May 10, 2025. This approach aligns with the preprocessing steps outlined in the earlier work to isolate Pc5 ULF wave signals (1.67-

6.7 mHz) by removing longer-period trends. We also investigated whether a 30-min running average, combined with a 60-min Fast Fourier Transform (FFT) window, could introduce artifacts in the statistical analysis of narrowband Pc5 waves, potentially generating spurious peaks at frequencies such as 0.8, 1.9, 2.9 mHz due to the response function of the MFA coordinate conversion[52]. However, the frequency histograms of the radial, azimuthal, and parallel components exhibit no significant excess peaks at these frequencies, suggesting that the MFA transformation and baseline determination do not introduce notable artifacts. This absence of excess peaks has been verified across the 30-year dataset, and we conclude that the chosen methodology does not compromise the integrity of the Pc5 wave detection. Invalid data points, such as those exceeding physically reasonable thresholds (e.g., magnetic field values $|B| > 1024$ nT or orbital parameters outside expected ranges), were marked as NaN. For orbital data (latitude, longitude, radius), outliers were identified and removed using the interquartile range (IQR) method, where data points outside the range [Q1−1.5 × IQR, Q3 + 1.5 × IQR] were excluded, with Q1 and Q3 being the 25th and 75th percentiles, respectively. This approach typically removes extreme values (e.g., <5% of data) while retaining the central 50% and other valid data. Magnetic field data from GOES-8 to GOES-15, available at 1-min cadence, were used as provided, while high-resolution data (10 Hz) from GOES-16 to GOES-18 were resampled to 1-min bins by computing the mean of all valid data points within each minute. This resampling ensures consistency across all satellites and facilitates Pc5 wave analysis, which requires a uniform time resolution. For the wave analysis, 1-h sliding windows (with 0.5-h overlap) were used, and windows containing any NaN values in the magnetic field components (B_r, B_ϕ, $B_{||}$) were excluded to ensure reliable Fourier analysis. Gaps in retained windows were not permitted, but for spectral analysis, a Hanning window was applied to mitigate edge effects, and signals were padded to a fixed length of 1440 points for standardized Fourier transforms. A fifth-order Butterworth high-pass filter with a 30-min cutoff period was applied to isolate Pc5 wave signals (1.6–6.7 mHz).

Pc5 ULF waves were detected using an enhanced CLEAN algorithm[23,53]. For each 1-h sliding window with a 0.5-h overlap, a Hanning window was applied, and the signal was zero-padded to 1440 points for consistent FFT resolution. The algorithm iteratively identified up to 50 peak frequencies per component as a safeguard against excessive iterations, typically finding far fewer (e.g., 3–5) significant peaks by fitting a Hanning peak model to refine frequency and amplitude estimates. The fitted model was subtracted from the power spectrum in each iteration to isolate subsequent peaks, with amplitudes calculated as $(4/N \cdot |\mathrm{FFT}|)$ at the peak frequency, where (N) is the number of data points, accounting for the Hanning window's normalization to estimate the wave's physical amplitude in nT. Peaks exceeding a 95% confidence level, determined via 5000 Monte Carlo white noise simulations, were selected within the Pc5 band.

Because the data were high-pass filtered with a 30-min cutoff and restricted to the 1.67–6.7 mHz Pc5 band, the steep $1/f^{\alpha}$ background present at lower frequencies was removed. As a result, the residual noise in this band is effectively white, justifying the use of white-noise surrogates for significance testing. The three highest-amplitude peaks per window were retained, yielding 27,279 radial, 26,145 azimuthal, and 31,259 parallel wave events for analysis across magnetic local time (MLT) and solar wind conditions. Following Murphy et al.[25], each detection in a single 1-h sliding window was counted as one event; if a peak persisted across overlapping windows, it was treated as multiple events, ensuring consistency with established statistical surveys of Pc5 ULF waves.

Solar wind condition separation

ULF wave events were categorized by solar wind conditions using hourly OMNI data from GSFC/SPDF OMNIWeb. We calculated the first and third quartiles (Q1, Q3) for solar wind speed (v_{sw}), dynamic pressure (P_{dyn}), and GSM B_z. Strong conditions were defined as $v_{sw} \geq 595$ km/s, $B_z \leq -3.5$ nT, and $P_{dyn} \geq 4.26$ nPa; weak conditions as $v_{sw} < 413$ km/s, $B_z > 1.6$ nT, and $P_{dyn} < 1.77$ nPa; and moderate conditions as intermediate values.

For long-term correlation analysis (Fig. 4), we use yearly averaged $|B_z|$ values to capture overall variability. Polarity reversals cancel in annual means, so using the magnitude avoids underestimating correlations. In contrast, in the condition-separated analysis we explicitly use signed B_z thresholds (negative $B_z \leq -3.5$ nT) to capture geoeffective southward fields. Thus, mixing of positive/negative B_z does not occur in the short-term condition separation.

Temporal occurrence rate analysis

ULF wave occurrence rates were calculated as the total number of significant Pc5 detections per year, where each day's count already integrates over a fixed set of 47 sliding 1-h windows (1-h length with 30-min overlap). The annual total was then normalized by the total number of available daily data records in that year across all contributing satellites, ensuring consistency despite differences in data coverage.

To examine short-term variability, we applied a fifth-order Butterworth high-pass filter with a cutoff frequency of 1/5 year^{-1}. This timescale follows Inceoglu et al.[46], which demonstrated that, on sub-5-year timescales, heliospheric conditions are dominated primarily by solar wind-driven processes rather than the more slowly evolving solar magnetic cycle. Filtering at this scale effectively removes the dominant 11-year solar cycle trend while retaining quasi-biennial oscillations (QBOs) with typical timescales of ∼1.5– years, allowing us to isolate the variability most directly linked to solar wind forcing (Fig. 4).

Frequency binning for power-law fits

To derive amplitude-frequency relationships, Pc5 ULF wave frequencies (1.67–6.7 mHz) were binned into 20 equal intervals. For each bin, median amplitudes were calculated across four MLT sectors (dawn: 3–9, day: 9–15, dusk: 15–21, night: 21–3 MLT) and three solar wind conditions (strong, moderate, weak). These binned data were used to fit power-law models, as shown in Figs. 2 and 3.

Data availability

The GOES MAG data used in this study were obtained from the National Centers for Environmental Information (NCEI): https://www.ncei.noaa.gov/products/space-weather/satellites

Received: 3 June 2025; Accepted: 15 September 2025
Published online: 21 October 2025

References

1. Jacobs, J. A., Kato, Y., Matsushita, S. & Troitskaya, V. A. Classification of geomagnetic micropulsations. *J. Geophys. Res.* **1896–1977**(69), 180–181 (1964) https://agupubs.onlinelibrary.wiley.com/doi/abs/10.1029/JZ069i001p00180.
2. Dungey, J. W. & Southwood, D. J. Ultra low frequency waves in the magnetosphere. *Space Sci. Rev.* **10**, 672–688 (1970).
3. Singer, H. J., Russell, C. T., Kivelson, M. G., Greenstadt, E. W. & Olson, J. V. Evidence for the control of pc 3,4 magnetic pulsations by the solar wind velocity. *Geophys. Res. Lett.* **4**, 377–379 (1977) https://agupubs.onlinelibrary.wiley.com/doi/abs/10.1029/GL004i009p00377.
4. Greenstadt, E. W., Singer, H. J., Russell, C. T. & Olson, J. V. Imf orientation, solar wind velocity, and pc 3–4 signals: A joint distribution. *J. Geophys. Res. Space Physics* **84**, 527–532 (1979) https://agupubs.onlinelibrary.wiley.com/doi/abs/10.1029/JA084iA02p00527.
5. Greenstadt, E., Olson, J., Loewen, P., Singer, H. & Russell, C. Correlation of pc 3, 4, and 5 activity with solar wind speed. *J. Geophys. Res. Space Physics* **84**, 6694–6696 (1979) https://agupubs.onlinelibrary.wiley.com/doi/abs/10.1029/JA084iA11p06694.
6. Chen, L. & Hasegawa, A. A theory of long-period magnetic pulsations: 2. impulse excitation of surface eigenmode. *J. Geophys. Res.* **1896–1977**(79), 1033–1037 (1974) https://agupubs.onlinelibrary.wiley.com/doi/abs/10.1029/JA079i007p01033.
7. Walker, A. D. M. The Kelvin-Helmholtz instability in the low-latitude boundary layer. *Planet. Space Sci.* **29**, 1119–1133 (1981).
8. Mathie, R. A. & Mann, I. R. On the solar wind control of Pc5 ULF pulsation power at mid-latitudes: Implications for MeV electron acceleration in the outer radiation belt. *J. Geophys. Res.* **106**, 29783–29796 (2001).
9. Hasegawa, H. et al. Kelvin-Helmholtz waves at the Earth's magnetopause: Multiscale development and associated reconnection. *J. Geophys. Res. (Space Phys.)* **114**, A12207 (2009).
10. Takahashi, K. & Ukhorskiy, A. Y. Solar wind control of Pc5 pulsation power at geosynchronous orbit. *J. Geophys. Res. (Space Phys.)* **112**, A11205 (2007).
11. Takahashi, K. & Ukhorskiy, A. Y. Timing analysis of the relationship between solar wind parameters and geosynchronous Pc5 amplitude. *J. Geophys. Res. (Space Phys.)* **113**, A12204 (2008).
12. Kessel, R. L. Solar wind excitation of Pc5 fluctuations in the magnetosphere and on the ground. *J. Geophys. Res. (Space Phys.)* **113**, A04202 (2008).
13. Southwood, D. J. A general approach to low-frequency instability in the ring current plasma. *J. Geophys. Res.* **81**, 3340 (1976).
14. Yamakawa, T. et al. Excitation of two types of storm-time pc5 ulf waves by ring current ions based on the magnetosphere-ionosphere coupled model. *J. Geophys. Res.: Space Phys.* **127**, e2022JA030486 (2022).
15. Kessel, R., Mann, I., Fung, S., Milling, D. & O'Connell, N. Correlation of Pc5 wave power inside and outside the magnetosphere during high speed streams. *Ann. Geophys.* **22**, 629–641 (2004).
16. Archer, M. O., Hartinger, M. D. & Horbury, T. S. Magnetospheric, magic frequencies as magnetopause surface eigenmodes. *Geophys. Res. Lett.* **40**, 5003–5008 (2013) https://agupubs.onlinelibrary.wiley.com/doi/abs/10.1002/grl.50979.
17. Liou, K., Takahashi, K., Newell, P. T. & Yumoto, K. Polar ultraviolet imager observations of solar wind-driven ulf auroral pulsations. *Geophys. Res. Lett.* https://doi.org/10.1029/2008GL034953 (2008).
18. Matteo, S., Villante, U., Viall, N., Kepko, L. & Wallace, S. On differentiating multiple types of ulf magnetospheric waves in response to solar wind periodic density structures. *J. Geophys. Res.: Space Phys.* **127**, e2021JA030144 (2022).
19. Viall, N. M., Kepko, L. & Spence, H. E. Relative occurrence rates and connection of discrete frequency oscillations in the solar wind density and dayside magnetosphere. *J. Geophys. Res.: Space Phys.* https://doi.org/10.1029/2008JA013334 (2009).
20. Hartinger, M. D., Turner, D. L., Plaschke, F., Angelopoulos, V. & Singer, H. The role of transient ion foreshock phenomena in driving pc5 ulf wave activity. *J. Geophys. Res. Space Physics* **118**, 299–312 (2013) https://agupubs.onlinelibrary.wiley.com/doi/abs/10.1029/2012JA018349.
21. Elkington, S. R. *A Review of ULF Interactions with Radiation Belt Electrons*, 177–193 (American Geophysical Union (AGU), 2006). urlhttps://agupubs.onlinelibrary.wiley.com/doi/abs/10.1029/169GM12.
22. Chen, L. & Hasegawa, A. A theory of long-period magnetic pulsations: 1. Steady state excitation of field line resonance. *J. Geophys. Res.* **79**, 1024–1032 (1974).
23. Loto'aniu, P. T. M. & Inceoglu, F. The distribution of pc5 ultralow-frequency waves at geostationary orbit. *Astrophys. J.* **969**, 91. https://doi.org/10.3847/1538-4357/ad41dd (2024).
24. Anderson, B. J. Ultra-low-frequency magnetic pulsations in the Earth's magnetosphere. *J. Hopkins APL Tech. Dig.* **11**, 239–254 (1990).
25. Murphy, K. R., Inglis, A. R., Sibeck, D. G., Watt, C. E. J. & Rae, I. J. Inner magnetospheric ULF waves: the occurrence and distribution of broadband and discrete wave activity. *J. Geophys. Res. (Space Phys.)* **125**, e27887 (2020).
26. Sarris, T. E. et al. Distribution of ULF wave power in magnetic latitude and local time using THEMIS and arase measurements. *J. Geophys. Res. (Space Phys.)* **127**, e2022JA030469 (2022).
27. Kokubun, S. Statistical characteristics of Pc-5 waves at geostationary orbit. *J. Geomagn. Geoelectr.* **37**, 759–779 (1985).
28. Zhu, X. & Kivelson, M. G. Compressional ULF waves in the outer magnetosphere 1. Statistical study. *J. Geophys. Res.* **96**, 19451–19467 (1991).
29. Cao, M., McPherron, R. L. & Russell, C. T. Statistical study of ULF wave occurrence in the dayside magnetosphere. *J. Geophys. Res.* **99**, 8731–8754 (1994).
30. Lessard, M. R., Hudson, M. K. & Lühr, H. A statistical study of Pc3-Pc5 magnetic pulsations observed by the AMPTE/Ion Release Module satellite. *J. Geophys. Res.* **104**, 4523–4538 (1999).
31. Viall, N. M., Kepko, L. & Spence, H. E. Relative occurrence rates and connection of discrete frequency oscillations in the solar wind density and dayside magnetosphere. *J. Geophys. Res.: Space Phys.* https://doi.org/10.1029/2008JA013334 (2009).
32. Liu, W. et al. Solar wind influence on pc4 and pc5 ulf wave activity in the inner magnetosphere. *J. Geophys. Res.: Space Phys.* https://doi.org/10.1029/2010JA015299 (2010).
33. Hartinger, M. D. et al. Properties of magnetohydrodynamic normal modes in the earth's magnetosphere. *J. Geophys. Res.: Space Phys.* **128**, e2023JA031987 (2023).
34. Rubtsov, A. V., Nosé, M., Matsuoka, A., Shinohara, I. & Miyoshi, Y. Polarization and spatial distribution features of pc4 and pc5 waves in the magnetosphere. *J. Geophys. Res.: Space Phys.* **128**, e2023JA031674 (2023).
35. Takahashi, K., Lee, D.-H., Merkin, V. G., Lyon, J. G. & Hartinger, M. D. On the origin of the dawn-dusk asymmetry of toroidal pc5 waves. *J. Geophys. Res. Space Phys.* **121**, 9632–9650 (2016) https://agupubs.onlinelibrary.wiley.com/doi/abs/10.1002/2016JA023009.
36. Mende, S. B., Frey, H. U., Morsony, B. J. & Immel, T. J. Statistical behavior of proton and electron auroras during substorms. *J. Geophys. Res.: Space Phys.* **108**, 5. https://doi.org/10.1029/2002JA009751 (2003).

37. Gerard, J.-C., Hubert, B., Grard, A., Meurant, M. & Mende, S. B. Solar wind control of auroral substorm onset locations observed with the image-fuv imagers. *J. Geophys. Res.: Space Phys.* **109**, 5. https://doi.org/10.1029/2003JA010129 (2004).
38. Frey, H. U., Mende, S. B., Angelopoulos, V. & Donovan, E. F. Substorm onset observations by image-fuv. *J. Geophys. Res.: Space Phys.* **109**, 6. https://doi.org/10.1029/2004JA010607 (2004).
39. Plaschke, F. *ULF Waves at the Magnetopause*, Ch. 12, 193–212 (American Geophysical Union (AGU), 2016). https://agupubs.onlinelibrary.wiley.com/doi/abs/10.1002/9781119055006.ch12.
40. Kavosi, S., Raeder, J., Johnson, J. R., Nykyri, K. & Farrugia, C. J. Seasonal and diurnal variations of Kelvin-Helmholtz Instability at terrestrial magnetopause. *Nat. Commun.* **14**, 2513 (2023).
41. Liu, W. et al. Electric and magnetic field observations of pc4 and pc5 pulsations in the inner magnetosphere: A statistical study. *J. Geophys. Res.: Space Phys.* https://doi.org/10.1029/2009JA014243 (2009).
42. Gorney, D. J. Solar cycle effects on the near-earth space environment. *Rev. Geophys.* **28**, 315–336 (1990).
43. Mann, I. R., O'Brien, T. P. & Milling, D. K. Correlations between ULF wave power, solar wind speed, and relativistic electron flux in the magnetosphere: solar cycle dependence. *J. Atmos. Solar Terr. Phys.* **66**, 187–198 (2004).
44. Zhang, J. et al. A statistical comparison of solar wind sources of moderate and intense geomagnetic storms at solar minimum and maximum. *J. Geophys. Res.: Space Phys.* https://doi.org/10.1029/2005JA011065 (2006).
45. Murphy, K. R., Mann, I. R., Rae, I. J. & Milling, D. K. Dependence of ground-based Pc5 ULF wave power on F10.7 solar radio flux and solar cycle phase. *J. Atmos. Solar Terr. Phys.* **73**, 1500–1510 (2011).
46. Inceoglu, F., Pacini, A. A. & Loto'aniu, P. T. M. Utilizing AI to unveil the nonlinear interplay of convection, drift, and diffusion on galactic cosmic ray modulation in the inner heliosphere. *Sci. Rep.* **12**, 20712 (2022).
47. Inceoglu, F. & Loto'aniu, P. T. M. Detection of solar QBO-like signals in earth's magnetic field from multi-GOES mission data. *Sci. Rep.* **13**, 19460 (2023).
48. Inceoglu, F., Simoniello, R., Arlt, R. & Rempel, M. Constraining non-linear dynamo models using quasi-biennial oscillations from sunspot area data. *Astron. Astrophys.* **625**, A117 (2019).
49. Inceoglu, F., Howe, R. & Loto'aniu, P. T. M. The Quasi-biennial-oscillation-type Signals in the Subsurface Flow Fields during Solar Cycles 23 and 24. *Astrophys J.* **920**, 49 (2021).
50. Inceoglu, F., Howe, R. & Loto'aniu, P. T. M. Causal interaction between the subsurface rotation rate residuals and radial magnetic field in different timescales. *Astrophys J.* **925**, 170 (2022).
51. Singer, H. J. & Kivelson, M. G. The latitudinal structure of Pc 5 waves in space: Magnetic and electric field observations. *J. Geophys. Res.* **84**, 7213–7222 (1979).
52. Matteo, S. & Villante, U. The identification of waves at discrete frequencies at the geostationary orbit: The role of the data analysis techniques and the comparison with solar wind observations. *J. Geophys. Res. Space Phys.* **123**, 1953–1968 (2018) https://agupubs.onlinelibrary.wiley.com/doi/abs/10.1002/2017JA024922.
53. Högbom, J. A. Aperture synthesis with a non-regular distribution of interferometer baselines. *Astron. Astrophys., Suppl. Ser.* **15**, 417 (1974).

Acknowledgements
The authors thank Juan Rodriguez and Howard Singer for their comments on the manuscript.

Author contributions
FI performed data preprocessing, conducted the analyses, interpreted the results, and wrote the manuscript. PTML supervised the study and contributed to the main body of the manuscript.

Funding
This research was supported in part by NOAA cooperative agreement NA22OAR4320151. The statements, findings, conclusions, and recommendations are those of the authors and do not necessarily reflect the views of NOAA or the U.S. Department of Commerce.

Declarations

Competing interests
The authors declare no competing interests.

Additional information
Correspondence and requests for materials should be addressed to F.I.

Reprints and permissions information is available at www.nature.com/reprints.

Publisher's note Springer Nature remains neutral with regard to jurisdictional claims in published maps and institutional affiliations.